Journal of Computational Physics 252 (2013) 290–309

Contents lists available at SciVerse ScienceDirect

Journal of Computational Physics

www.elsevier.com/locate/jcp

A diffuse interface model with immiscibility preservation

Arpit Tiwari [a], Jonathan B. Freund [a,b,*], Carlos Pantano [a]

[a] Department of Mechanical Science and Engineering, University of Illinois at Urbana-Champaign, Urbana, IL 61801, USA
[b] Department of Aerospace Engineering, University of Illinois at Urbana-Champaign, Urbana, IL 61801, USA

ARTICLE INFO

Article history:
Received 12 January 2013
Received in revised form 10 June 2013
Accepted 15 June 2013
Available online 27 June 2013

Keywords:
Multiphase flows
Numerical diffusion
Interface capturing
Diffuse interface model
Bubble collapse

ABSTRACT

A new, simple, and computationally efficient interface capturing scheme based on a diffuse interface approach is presented for simulation of compressible multiphase flows. Multi-fluid interfaces are represented using field variables (interface functions) with associated transport equations that are augmented, with respect to an established formulation, to enforce a selected interface thickness. The resulting interface region can be set just thick enough to be resolved by the underlying mesh and numerical method, yet thin enough to provide an efficient model for dynamics of well-resolved scales. A key advance in the present method is that the interface regularization is asymptotically compatible with the thermodynamic mixture laws of the mixture model upon which it is constructed. It incorporates first-order pressure and velocity non-equilibrium effects while preserving interface conditions for equilibrium flows, even within the thin diffused mixture region. We first quantify the improved convergence of this formulation in some widely used one-dimensional configurations, then show that it enables fundamentally better simulations of bubble dynamics. Demonstrations include both a spherical-bubble collapse, which is shown to maintain excellent symmetry despite the Cartesian mesh, and a jetting bubble collapse adjacent a wall. Comparisons show that without the new formulation the jet is suppressed by numerical diffusion leading to qualitatively incorrect results.

© 2013 Elsevier Inc. All rights reserved.

1. Introduction

Aspherical-bubble dynamics has been studied extensively using boundary integral numerical method [1–9]. Since this formulation is for incompressible fluids, it must therefore be supplemented, when feasible, with additional models whenever compressibility effects are important. For example, in violent collapses, artificial energy extraction is needed to account for the substantial energy lost to acoustic emission [9]. In bubble-cluster collapse, it is known that these same pressure pulses affect the dynamics of nearby bubbles [10,11]. This limitation motivates the development of methods that explicitly include compressibility. Unfortunately, it is often difficult for compressible flow formulations to ensure that the interface between the liquid and the gas remains realistically sharp, especially given the dissipation inherent in shock-capturing schemes. A challenge in any multiphase compressible numerical method is the simultaneous and faithful representation of both shocks and interfaces.

One class of compressible multiphase flow approaches is Lagrangian, which includes arbitrary Lagrangian–Eulerian [12], free-Lagrange [13,14], and front tracking methods [15–18]. These maintain sharp interfaces via explicit representation, but they introduce geometric complexity for large deformations and topological changes. A level-set [19,20] based Eulerian approach coupled with the ghost fluid technique mitigates topological difficulties [21,22]. However, the method requires special

* Corresponding author at: Department of Mechanical Science and Engineering, University of Illinois at Urbana-Champaign, Urbana, IL 61801, USA.
E-mail addresses: atiwari2@illinois.edu (A. Tiwari), jbfreund@illinois.edu (J.B. Freund), cpantano@illinois.edu (C. Pantano).
URLs: http://jbfreund.mechse.illinois.edu/ (J.B. Freund), http://eurus.mechse.illinois.edu/ (C. Pantano).

0021-9991/$ – see front matter © 2013 Elsevier Inc. All rights reserved.
http://dx.doi.org/10.1016/j.jcp.2013.06.021

thermodynamic management at the interface for flows with high density or pressure ratios [23–31]. Another way to cope with the geometric challenges of Lagrangian tracking is to allow the interface to artificially diffuse into thin zones where multiple fluids overlap, forming in effect a mixture region. Multiphase flow theory is invoked to define thermodynamic variables in these mixture zones [32–42]. To be consistent with the nominally discontinuous interface of an actual immiscible fluid, these zones should be thinner than the features of the flow. In the well-known "single-fluid" model, this description is implemented by augmenting the Euler equations with equations that describe the evolution of smooth functions that mark different fluids [43–49].

There are two main challenges specific to the diffuse interface approach: (1) obtaining consistent thermodynamic laws for the mixture, and (2) preventing artificial spatial distortions of the interface functions. These two challenges are coupled as we demonstrate for the bubble collapse configuration in Section 2. The second of these challenges is the more obvious. Without correction, distortions make the interface either too sharp to be represented on the mesh or so diffuse that it is no longer thin relative to other relevant flow features. Furthermore, it is also widely recognized that inconsistent interface thermodynamics can lead to mechanical incompatibilities. Mixture models obtained by asymptotic reduction of the Baer–Nunziato non-equilibrium multiphase model [32,33] under stiff mechanical relaxation [38,40,41] provide transport of interface functions consistent with first-order pressure and velocity non-equilibrium effects. Incorporation of first-order non-equilibrium effects constitutes a significant improvement, but the interfaces can still become so diffused and distorted without proper numerical regularization that key flow features can be completely lost. We will show in Section 2 and Section 5 that this level of thermodynamic consistency alone is insufficient, particularly when strain smears the interface, as for a near-wall bubble collapse. Such distortions can be countered with specially designed terms in the governing equations that cause the interface function transition to span an approximately constant-thickness zone, as proposed recently by Shukla et al. [50] for compressible flows. Unfortunately, these source terms are not necessarily compatible with the thermodynamic mixture models in the interface zone, which can lead to accumulation of errors in space and time, even far from the interface. So et al. [51] have recently developed an anti-diffusive method to address this problem. This technique, however, is intimately tied to the underlying numerical scheme and it is therefore difficult to generalize to different discretizations, such as an increase in the order of accuracy. There is also the risk that anti-diffusive fluxes can over-sharpen the interface in flow regions already drawn thin by the resolved strain field (discussed in Section 3 and Section 5.4). Alternatively, Kokh and Lagoutière [52] have shown encouraging results with an anti-diffusive Lagrange-Remap scheme that controls numerical diffusion via limited downwind fluxes in the remap stage. The method, however, requires additional steps to compute, and remap from, Lagrangian variables, and its extension to more general interfacial mixture laws has not been explored yet.

In this paper, we present a new mixture-consistent interface regularization approach that addresses the limitations identified in the previous discussion. It maintains the integrity of the thin interface between immiscible fluids with a sharpening term, but this term is now crafted in such a way that it remains consistent with the first-order non-equilibrium mixture model. This regularization operator is incorporated into the continuum model, making the overall model independent of the numerical scheme employed. For example, it is easily demonstrated on a standard shock-tube problem in one dimension, and is also directly compatible with a multi-resolution Adaptive Mesh Refinement (AMR) implementation and a fifth-order WENO scheme we use to demonstrate its properties for three-dimensional bubble collapse.

2. Motivation: mixture-zone models and discretization

Faced with the limited availability of exact solutions that can be used for comparison and analysis of our method, we frame our initial discussion on a free-space spherical-bubble collapse in a compressible liquid. In the weak compressibility limit, this configuration has a semi-analytic solution, obtained upon solving an ordinary differential equation [53,54], which we treat as nominally "exact". Though one-dimensional in the radial coordinate, the configuration is advantageous in that it can be used to evaluate simulations on a three-dimensional mesh, and thereby illustrate key features of methods that will be important for complex-geometry applications. If a method is unable to do this, there is little hope that more complex flows can be well approximated by such a computational model. We therefore use it to motivate the development of the proposed method, which we present in detail in Section 3.

In all the simulations, water is modeled with a stiffened-gas equation of state (see (10) in Section 3 where we present the formulation in detail) using $\gamma = 4.4$ and $p^\infty = 600$ MPa and air is modeled as an ideal gas with $\gamma = 1.4$ ($p^\infty = 0$ MPa). The simulation domain is a $40 \times 40 \times 40$ mm^3 cube with a bubble of initial radius $R_0 = 1$ mm at its center. The bubble is discretized with a mesh of minimum spacing $\Delta x_{\min}$ such that $\bar{R}_{\min}/\Delta x_{\min} \approx 13.9$, where $\bar{R}_{\min}$ is its minimum radius over the entire simulated time. Details of the initial conditions are provided in Section 5.2, where we present one-dimensional (radial coordinate) simulation results for this problem. Here, we compare six approaches on the same three-dimensional mesh:

($\tilde{\text{A}}$) Interface capturing based upon an established equilibrium mixture model without any interface regularization [39, 46–49];
(A) The model of Shukla et al. [50], which employs the two-fluid equilibrium model of Allaire et al. [39] and the interface regularization first proposed by Olsson and Kreiss [55] for incompressible flows;
(B) The method of So et al. [51], which employs anti-diffusive fluxes to sharpen the interface;
($\tilde{\text{B}}$) Method B without the anti-diffusive fluxes;

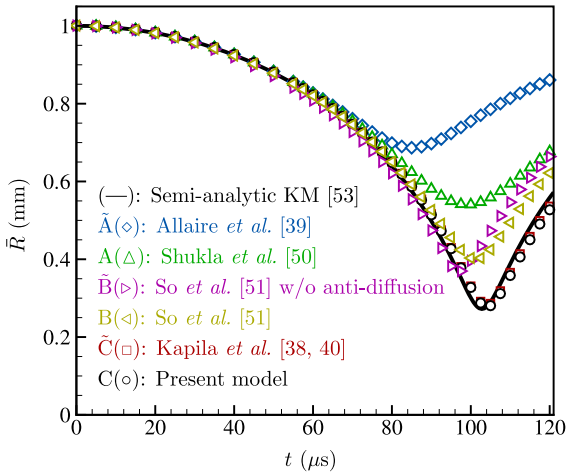

(a)

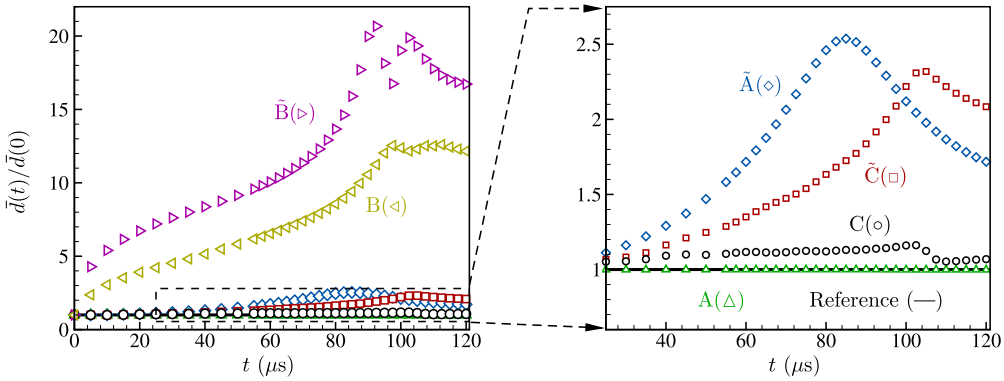

(b)

Fig. 1. Evolution of (a) radius $\bar{R}(t)$ defined in (1) and (b) thickness of the two-fluid interface $\bar{d}(t)$ defined in (2) relative to the initial thickness using models $\tilde{\mathrm{A}}$ (◇), A (△), $\tilde{\mathrm{B}}$ (▷), B (◁), $\tilde{\mathrm{C}}$ (□), and C (○) for isolated single-bubble collapse under a pressure ratio of 10. The results are compared with the semi-analytic KM [53] solution (−) in (a), and the desired constant interface thickness with exact immiscibility (−) in (b).

($\tilde{\mathrm{C}}$) The asymptotically reduced model of Kapila et al. [38,40], which includes first-order non-equilibrium effects without any interface regularization; and

(C) The new model, presented in detail in Section 3, which incorporates an interface regularization in a similar spirit to that we used previously [50], but is now consistent with first-order non-equilibrium effects [38,40] in the mixture zone. This demonstration will show how advantageous such consistency can be.

The numerical method used for solving models $\tilde{\mathrm{A}}$, A, $\tilde{\mathrm{C}}$ and C is detailed in Section 4. Since the anti-diffusion approach depends on the diffusion of the underlying solver, the numerical solver used for methods $\tilde{\mathrm{B}}$ and B is the same as that employed by So et al. [51]. (Method $\tilde{\mathrm{B}}$ is included in the analysis only to highlight the effect of anti-diffusion.) Fig. 1(a) compares the radius of the bubble from three-dimensional simulations with the Keller–Miksis (KM) [53] solution. The equivalent radius $\bar{R}(t)$ is defined in terms of the gas volume fraction α_2, according to

$$\frac{4}{3}\pi \bar{R}^3(t) = \iiint \alpha_2(\boldsymbol{x}, t)\, d\boldsymbol{x}, \tag{1}$$

where $\boldsymbol{x} = \{x, y, z\}$.

The equilibrium model $\tilde{\mathrm{A}}$ and our previous mixture-inconsistent model A both lead to rebound significantly earlier compared to the reference solution. In both cases, the assumption of total thermodynamic equilibrium at the interface increases the internal bubble pressure at an erroneously faster rate. Models $\tilde{\mathrm{C}}$ and C are far more accurate, providing a fundamentally better minimum radius and collapse time predictions on the same mesh as $\tilde{\mathrm{A}}$, A, $\tilde{\mathrm{B}}$ and B.

To assess the interface preservation property of different models, we compute the thickness

$$\bar{d}(t) = \frac{1}{\bar{S}(t)} \iiint \alpha_2(\boldsymbol{x}, t)\big[1 - \alpha_2(\boldsymbol{x}, t)\big]\, d\boldsymbol{x}, \tag{2}$$

where $\bar{S}(t)$ is the bubble surface area

$$\bar{S}(t) = \iiint \left|\nabla\alpha_2(\boldsymbol{x}, t)\right| d\boldsymbol{x}. \tag{3}$$

This definition yields the exact thickness d if the volume fraction obeys

$$\alpha_2 = \frac{1}{2}\left[1 - \tanh\left(\frac{r - R}{2d}\right)\right], \tag{4}$$

where R is the radial coordinate at which $\alpha_2 = 0.5$. As can be seen in Fig. 1(b), method $\tilde{\mathrm{B}}$ is the most diffusive; the anti-diffusive fluxes in method B reduce this. The regularization operator in our model C has a user-defined mesh-independent length-scale that governs the thickness of the interface. By construction, such a length-scale does not exist in the anti-diffusion approach. The thickness of the sharpened interface using B, therefore, does not remain fixed as it is determined by the dynamics of the flow.

Compared to A and C, models $\tilde{\mathrm{A}}$ and $\tilde{\mathrm{C}}$ significantly thicken the interface during collapse, with peak thickness smeared by more than a factor of two around the time of minimum volume. To maintain a thin interface relative to the corresponding interface features in a complex three-dimensional configuration, this would necessitate 8 times the mesh, and this situation would degrade further as the interface diffuses further throughout the course of a simulation. Models A and C, which use regularization to ensure the thickness is approximately constant, do not show this behavior. Model A, which does not respect self-consistent mixture rules, is modestly better than C in preserving fluid immiscibility, but is far inferior for the generally more important bubble radius history $\bar{R}(t)$ in Fig. 1(a). We also note in Fig. 1(a) that the radius history obtained using model C agrees well with that obtained using $\tilde{\mathrm{C}}$ upon which it is built. Therefore, our consistent interface regularization preserves large-scale features (associated with the bubble radius $\bar{R}$) while better resolving small-scale features (associated with the interface thickness $\bar{d}$). Such an agreement is clearly not observed for the interface sharpening methods A and B. It is thus clear that the proposed model C is advantageous for spherical-bubble collapse on a three-dimensional Cartesian grid, a model for any challenging complex simulation on a non-interface-conforming mesh. In making these comparisons for bubble collapse and rebound, we recognize that different methods are better suited to meet the diverse challenges presented by different classes of problems. There is no expectation that any method will be universally superior.

Since the new model C, which is formulated in the following section, is a continuum model, it is compatible with different underlying discretizations. Fig. 2 shows how the better resolution properties of a fifth-order WENO scheme, as an example, is advantageous despite its nominally equivalent low-order behavior at interfaces. We see in Figs. 2(a) and 2(b) that it is far more effective at maintaining the spherical symmetry of the bubble, which is confirmed quantitatively in Fig. 2(c), which shows the behavior of spherical harmonics. For spherical harmonics Y_l^m which satisfy

$$\frac{1}{4\pi}\int_0^{2\pi}\int_0^{\pi} Y_l^m(\theta,\phi) Y_{l'}^{m'}(\theta,\phi)\sin\theta\, d\theta\, d\phi = \delta_{ll'}\,\delta_{mm'}, \tag{5}$$

a Parseval equality provides a convenient measure of the spectrum,

$$\zeta_l^2 = \sum_{m=-l}^{l} r_{lm}^2, \tag{6}$$

where l and m represent degree and order of the spherical harmonic function, respectively, ζ_l denotes the power in mode l, and r_{lm} represents the coefficients corresponding to Y_l^m. To compute ζ_l, we first obtain the bubble radius $\hat{R}(\theta,\phi)$ defined by $\alpha_2 = 0.5$ from the three-dimensional simulations, then compute the coefficients r_{lm} using the SPHEREPACK library [56]. The clear superiority of fifth-order WENO will also benefit it in more complex configurations. The main advantage of the high-order method is that it has a much lower grid anisotropy error and therefore lowers the unavoidable directionality introduced by the Cartesian mesh. The more accurate (spherically symmetric) flow fields around the bubble yield a more accurate radius history, as seen in the inset of Fig. 2(d). Though these errors are small compared to the large errors seen for the different formulations in Fig. 1(a), the WENO scheme provides a significantly more accurate representation of the bubble radius.

3. Model formulation

The two-fluid model is developed starting with a variant [33] of the Baer–Nunziato model [32]. It assumes neither pressure nor velocity equilibrium at the interface, with separate conservation of mass, momentum, and energy equations for each fluid, along with an equation for the evolution of volume fraction (interface function) of one of the two fluids. We present the seven-equation model [33,40], in terms of entropy (s_k), velocity ($\mathbf{u}_k$), pressure (p_k), and volume fraction (α_k) of fluids $k = 1$ and 2,

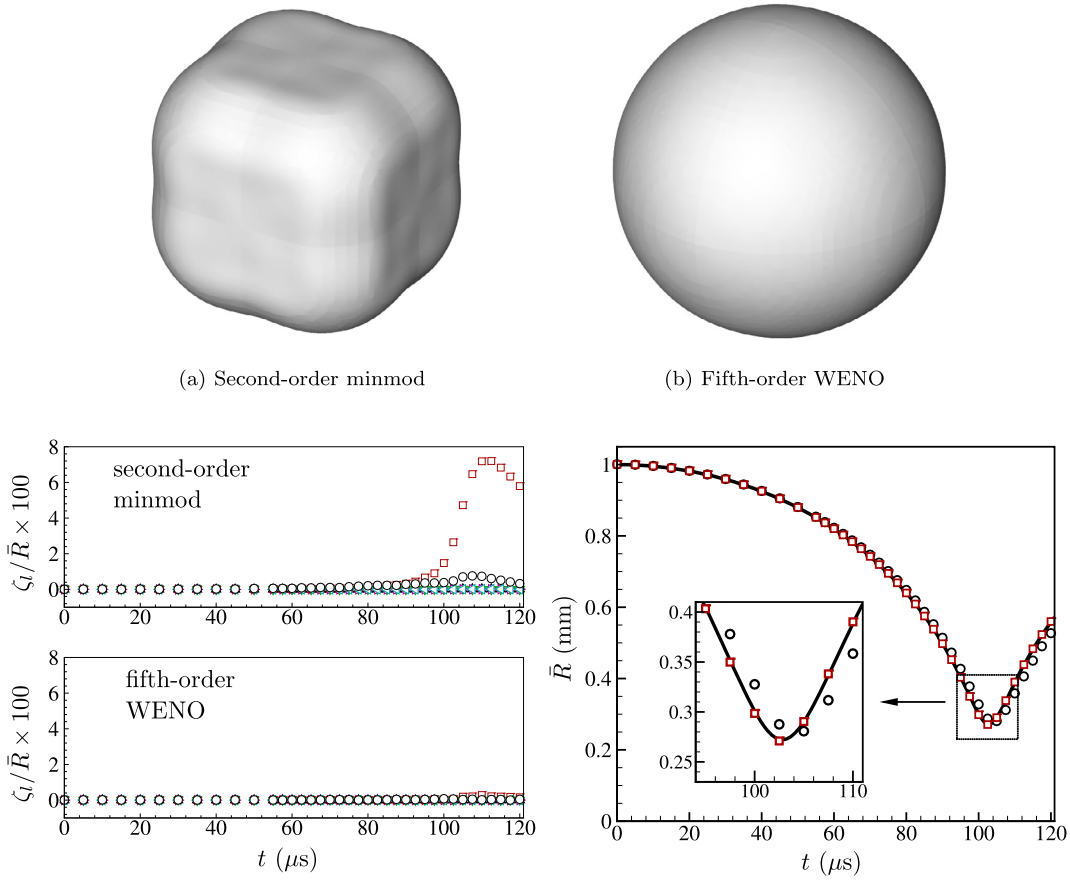

(a) Second-order minmod

(b) Fifth-order WENO

(c) Spherical harmonics power spectrum

(d) Radius history

Fig. 2. Bubble shapes obtained from model D using (a) second-order minmod and (b) fifth-order WENO at $t = 110$ μs for isolated single-bubble collapse under a pressure ratio of 10; (c) evolution of spherical harmonics power-spectrum for $l = 1$ (△), $l = 2$ (▽), $l = 3$ (▷), $l = 4$ (□), $l = 5$ (◁) and $l = 6$ (○); and (d) radius history using second-order minmod (○) and fifth-order WENO (□), compared with the Keller–Miksis [53] solution (–).

$$\alpha_1\rho_1 T_1 \frac{\mathrm{D}_1 s_1}{\mathrm{D}t} = (p_\mathrm{I} - p_1)(\mathbf{u}_\mathrm{I} - \mathbf{u}_1)\cdot\nabla\alpha_1 + \mu(p_\mathrm{I} - p_1)(p_2 - p_1) + \lambda(\mathbf{u}_\mathrm{I} - \mathbf{u}_1)\cdot(\mathbf{u}_2 - \mathbf{u}_1), \tag{7a}$$

$$\alpha_2\rho_2 T_2 \frac{\mathrm{D}_2 s_2}{\mathrm{D}t} = (p_\mathrm{I} - p_2)(\mathbf{u}_\mathrm{I} - \mathbf{u}_2)\cdot\nabla\alpha_2 + \mu(p_\mathrm{I} - p_2)(p_1 - p_2) + \lambda(\mathbf{u}_\mathrm{I} - \mathbf{u}_2)\cdot(\mathbf{u}_1 - \mathbf{u}_2), \tag{7b}$$

$$\alpha_1\rho_1 \frac{\mathrm{D}_1 \mathbf{u}_1}{\mathrm{D}t} + \nabla(\alpha_1 p_1) = p_\mathrm{I}\nabla\alpha_1 + \lambda(\mathbf{u}_2 - \mathbf{u}_1), \tag{7c}$$

$$\alpha_2\rho_2 \frac{\mathrm{D}_2 \mathbf{u}_2}{\mathrm{D}t} + \nabla(\alpha_2 p_2) = p_\mathrm{I}\nabla\alpha_2 + \lambda(\mathbf{u}_1 - \mathbf{u}_2), \tag{7d}$$

$$\alpha_1 \frac{\mathrm{D}_1 p_1}{\mathrm{D}t} + \alpha_1\rho_1 a_1^2 \nabla\cdot\mathbf{u}_1 = \rho_1 a_{1\mathrm{I}}^2(\mathbf{u}_\mathrm{I} - \mathbf{u}_1)\cdot\nabla\alpha_1 + \mu\rho_1 a_{1\mathrm{I}}^2(p_2 - p_1) + \lambda\sigma_1(\mathbf{u}_\mathrm{I} - \mathbf{u}_1)\cdot(\mathbf{u}_2 - \mathbf{u}_1), \tag{7e}$$

$$\alpha_2 \frac{\mathrm{D}_2 p_2}{\mathrm{D}t} + \alpha_2\rho_2 a_2^2 \nabla\cdot\mathbf{u}_2 = \rho_2 a_{2\mathrm{I}}^2(\mathbf{u}_\mathrm{I} - \mathbf{u}_2)\cdot\nabla\alpha_2 + \mu\rho_2 a_{2\mathrm{I}}^2(p_1 - p_2) + \lambda\sigma_2(\mathbf{u}_\mathrm{I} - \mathbf{u}_2)\cdot(\mathbf{u}_1 - \mathbf{u}_2), \tag{7f}$$

$$\frac{\mathrm{D}_\mathrm{I}\alpha_2}{\mathrm{D}t} = \mu(p_2 - p_1) + \mathcal{R}(\alpha_2). \tag{7g}$$

The new term $\mathcal{R}$ added to (7g) is a user specified regularization operator that sets the interface thickness; our specific $\mathcal{R}$ is defined in (20). The subscript I, appearing in the right-hand side of several of the equations, indicates an interface quantity. At this point, the interface velocity $\mathbf{u}_\mathrm{I}$ and pressure p_I are retained as distinct variables. Material derivatives for each fluid and the interface are

$$\frac{\mathrm{D}_l}{\mathrm{D}t} = \frac{\partial}{\partial t} + \mathbf{u}_l\cdot\nabla, \tag{8}$$

for $l = 1$, 2 and I. The fluid densities, temperatures and sound speeds are ρ_k, T_k and a_k, respectively. The mass-specific total energy is $E_k = e_k + |\mathbf{u}_k|^2/2$, where e_k is the mass-specific internal energy. The interfacial variables ($\mathbf{u}_\mathrm{I}$ and p_I) are, in general, obtained by weighted averaging of the respective quantities on either side of the interface [33], but the choice of averaging is not explicit in our formulation after we reduce the model to equilibrium velocity and pressure at the interface. The parameters λ and μ are the rates at which velocity and pressure relax to thermodynamic equilibrium, respectively, and

$$\sigma_k = \frac{1}{\rho_k}\left(\frac{\partial p_k}{\partial e_k}\right)_{\rho_k}. \tag{9}$$

The modified seven-equation non-equilibrium model (7a)–(7g), including the new $\mathcal{R}$ in (7g), is reduced consistently to the five-equation model under stiff mechanical relaxation. The assumption underlying this procedure is that the relaxation times for the velocities and pressures of the two fluids to reach equilibrium are small compared to the characteristic times of the flow, implying λ and $\mu \to \infty$. The procedure is lengthy, but straightforward; details are included in Appendix A. The reduced system (A.16a)–(A.16e) incorporates first-order mechanical non-equilibrium effects as well as the new, now thermodynamically self-consistent, interface regularization (Appendix A).

The analysis in Appendix A provides a consistent way of regularizing all the conservative variables by incorporating $\mathcal{R}$ in the continuum formulation, which distinguishes our model from the interface sharpening approaches of Shukla et al. [50] and So et al. [51]. In the approach of Shukla et al. [50], the density and interface function are sharpened first, then momentum and energy are discretely updated such that velocity and pressure in each cell remain unchanged. In the anti-diffusion method of So et al. [51], discrete sharpening fluxes for the conservative variables are obtained using the discrete anti-diffusive fluxes for volume fraction such that pressure and velocity equilibrium is maintained in each cell. Thermodynamic self-consistency guarantees that our continuum formulation (A.16a)–(A.16e), by construction, conserves specific entropies (s_k) of each phase under isentropic conditions along with preserving velocity and pressure equilibrium. The consistency of this regularization is shown in Section 2.

The asymptotic analysis that unifies this regularization is carried out for fluids whose states are fixed by two thermodynamic variables and is therefore broadly applicable. The stiffened-gas equation of state [57] provides a good model for our bubble dynamics application:

$$\rho_k e_k = \Gamma_k p_k + \Pi_k, \tag{10}$$

with

$$\Pi_k = \frac{\gamma_k p_k^\infty}{\gamma_k - 1}, \tag{11}$$

$$\Gamma_k = \frac{1}{\gamma_k - 1}, \tag{12}$$

where γ_k and p_k^∞ are the usual stiffened-gas parameters [57]. For this equation of state, the reduced system with consistent regularization (A.16a)–(A.16e) becomes

$$\frac{\partial \alpha_1\rho_1}{\partial t} + \nabla\cdot(\alpha_1\rho_1\mathbf{u}) = -\rho_1\mathcal{R}(\alpha_2), \tag{13a}$$

$$\frac{\partial \alpha_2\rho_2}{\partial t} + \nabla\cdot(\alpha_2\rho_2\mathbf{u}) = \rho_2\mathcal{R}(\alpha_2), \tag{13b}$$

$$\frac{\partial \rho\mathbf{u}}{\partial t} + \nabla\cdot(\rho\mathbf{u}\otimes\mathbf{u}) + \nabla p = (\rho_2 - \rho_1)\mathbf{u}\mathcal{R}(\alpha_2), \tag{13c}$$

$$\frac{\partial \rho E}{\partial t} + \nabla\cdot\big((\rho E + p)\mathbf{u}\big) = \big((\rho_2 - \rho_1)\kappa + p(\Gamma_2 - \Gamma_1) + \Pi_2 - \Pi_1\big)\mathcal{R}(\alpha_2), \tag{13d}$$

$$\frac{\partial \alpha_2}{\partial t} + \mathbf{u}\cdot\nabla\alpha_2 = \alpha_1\alpha_2\frac{\rho_1 a_1^2 - \rho_2 a_2^2}{\alpha_1\rho_2 a_2^2 + \alpha_2\rho_1 a_1^2}\nabla\cdot\mathbf{u} + \mathcal{R}(\alpha_2), \tag{13e}$$

where $\mathbf{u}$ and p are the equilibrium velocity and pressure (Appendix A),

$$\alpha_1 + \alpha_2 = 1, \tag{14}$$

$$\rho = \alpha_1\rho_1 + \alpha_2\rho_2, \tag{15}$$

$$\rho E = \alpha_1\rho_1 E_1 + \alpha_2\rho_2 E_2, \tag{16}$$

$$\kappa = \frac{1}{2}|\mathbf{u}|^2. \tag{17}$$

The mixture speed of sound a is obtained using

$$\frac{1}{\rho a^2} = \frac{\alpha_1}{\rho_1 a_1^2} + \frac{\alpha_2}{\rho_2 a_2^2}, \tag{18}$$

which reflects the eigenvalues of the hyperbolic part of the reduced system, (A.16a)–(A.16e). Any other averaging to obtain the mixture sound speed (frozen sound speed [42], for example) would be inconsistent with (A.16a)–(A.16e). For stiffened gases, the phasic sound speeds (a_k) are given by

$$a_k = \sqrt{\gamma_k \frac{p + p_k^\infty}{\rho_k}}. \tag{19}$$

The specification of $\mathcal{R}$ completes the system. The goal is to represent the interface with a smeared Heaviside function of constant and uniform thickness throughout the simulation. For incompressible multi-fluid flows, Olsson et al. [55,58] used the hyperbolic tangent as the smeared Heaviside function. For compressible flows, Shukla et al. [50] proposed a modified form that has been shown to work well for the diffuse interface methods based on the advection model [39]. We use a similar operator in this study for the asymptotically reduced model,

$$\mathcal{R}(\alpha_2) = \mathcal{L}(\alpha_2)\,\mathcal{U}_0\,\mathbf{n}\cdot\nabla\big(\epsilon|\nabla\alpha_2| - \alpha_2(1-\alpha_2)\big), \tag{20}$$

where the balance of interface sharpening ($\alpha_2(1-\alpha_2)$) and diffusion ($\epsilon|\nabla\alpha_2|$) fluxes maintains the interface thickness. The parameter ϵ, which is of the order of the grid spacing but controlled explicitly by the user, defines the thickness of the interface, and $\mathcal{U}_0$ represents the characteristic regularization rate. The interface normal,

$$\mathbf{n} = \nabla\alpha_2/|\nabla\alpha_2|, \tag{21}$$

directs the operation across the interface, and

$$\mathcal{L}(\alpha_2) = \begin{cases} 1 & \text{for } 10^{-6} < \alpha_2 < 1 - 10^{-6}, \\ 0 & \text{otherwise.} \end{cases} \tag{22}$$

Since the distortions of the interface function field are largely driven by the velocity field near the interface, it is convenient to choose $\mathcal{U}_0 = \|\mathbf{u}_\mathrm{I}\|_{\max}$. We obtain an estimate of $\|\mathbf{u}_\mathrm{I}\|_{\max}$ using:

$$\|\mathbf{u}_\mathrm{I}\|_{\max} = \frac{(\alpha_2(1-\alpha_2)|\mathbf{u}|)_{\max}}{(\alpha_2(1-\alpha_2))_{\max}} = 4\left(\alpha_2(1-\alpha_2)|\mathbf{u}|\right)_{\max}. \tag{23}$$

Having ϵ as an independent length-scale is advantageous. The terms $\mathbf{u}\cdot\nabla\alpha_2$ and $\beta\nabla\cdot\mathbf{u}$ in (A.16e) both can thicken or thin the interface. While regularization schemes are usually designed with interface sharpening in mind to counter the smearing of numerical diffusion, a purely sharpening term does not prevent over-thinning the interface when it works in concert with an interface-thinning strain. In the absence of such a length-scale, especially if there is complex flow, strain can disrupt the balance between the numerical diffusion and the artificial anti-diffusion. Relying on the mesh size rather than ϵ is also ill-suited for AMR-WENO, because the usual refinement criteria are predicated on the mesh-independence of the underlying solution.

It should also be noted that computation of phase densities for the right-hand side of (13a)–(13e) using the standard formula $\rho_k = \alpha_k\rho_k/\alpha_k$ could lead to spurious oscillatory behavior near the interface where both $\alpha_k\rho_k$ and α_k have large gradients. To make the formulation more robust, we consider the assumption that phase densities ρ_k, though not of course the mixture density ρ, vary slowly across the interface in the computation of regularization terms

$$\frac{\partial\rho_k}{\partial n} \approx 0. \tag{24}$$

With this approximation, we avoid the explicit computation of ρ_k in the right-hand side of (13a)–(13e). To this end, we first take the gradient of $\rho_k\alpha_k$,

$$\nabla(\rho_k\alpha_k) = \rho_k\nabla\alpha_k + \alpha_k\nabla\rho_k, \tag{25}$$

then, using (14) and (24), we obtain

$$\mathbf{n}\cdot\nabla(\rho_2\alpha_2) \approx \rho_2\mathbf{n}\cdot\nabla\alpha_2, \tag{26a}$$

$$\mathbf{n}\cdot\nabla(\rho_1\alpha_1) \approx -\rho_1\mathbf{n}\cdot\nabla\alpha_2. \tag{26b}$$

Subsequently, we use (21) and (26a), (26b) to develop an approximation for the first term of $\rho_k\mathcal{R}(\alpha_2)$ in (13a) and (13b)

$$\rho_2|\nabla\alpha_2| \approx \mathbf{n}\cdot\nabla(\rho_2\alpha_2), \tag{27a}$$

$$-\rho_1|\nabla\alpha_2| \approx \mathbf{n}\cdot\nabla(\rho_1\alpha_1), \tag{27b}$$

and for the second term

$$\rho_k \mathbf{n} \cdot \nabla\big(\alpha_k(1-\alpha_k)\big) \approx (1-2\alpha_k)\mathbf{n} \cdot \nabla(\rho_k \alpha_k). \tag{28}$$

From (27a), (27b) and (28), we get

$$\rho_2 \mathcal{R}(\alpha_2) \approx \mathcal{L}(\alpha_2)\mathcal{U}_0 \mathbf{n} \cdot \big(\nabla\big(\epsilon\, \mathbf{n} \cdot \nabla(\rho_2\alpha_2)\big) - (1-2\alpha_2)\nabla(\rho_2\alpha_2)\big) \equiv \hat{\mathcal{R}}_2(\rho_2\alpha_2, \alpha_2), \tag{29a}$$

$$-\rho_1 \mathcal{R}(\alpha_2) \approx \mathcal{L}(\alpha_2)\mathcal{U}_0 \mathbf{n} \cdot \big(\nabla\big(\epsilon\, \mathbf{n} \cdot \nabla(\rho_1\alpha_1)\big) - (1-2\alpha_2)\nabla(\rho_1\alpha_1)\big) \equiv \hat{\mathcal{R}}_1(\rho_1\alpha_1, \alpha_2). \tag{29b}$$

Substituting these $\hat{\mathcal{R}}_k$ for $\rho_k\mathcal{R}$ in (13a)–(13e) yields the specific quasi-conservative system we use:

$$\frac{\partial \rho_1\alpha_1}{\partial t} + \nabla \cdot (\rho_1\alpha_1\mathbf{u}) = \hat{\mathcal{R}}_1, \tag{30a}$$

$$\frac{\partial \rho_2\alpha_2}{\partial t} + \nabla \cdot (\rho_2\alpha_2\mathbf{u}) = \hat{\mathcal{R}}_2, \tag{30b}$$

$$\frac{\partial \rho\mathbf{u}}{\partial t} + \nabla \cdot (\rho\mathbf{u} \otimes \mathbf{u}) + \nabla p = \mathbf{u}\hat{\mathcal{R}}, \tag{30c}$$

$$\frac{\partial \rho E}{\partial t} + \nabla \cdot \big((\rho E + p)\mathbf{u}\big) = \kappa\,\hat{\mathcal{R}} + \big(p(\Gamma_2 - \Gamma_1) + \Pi_2 - \Pi_1\big)\mathcal{R}, \tag{30d}$$

$$\frac{\partial \alpha_2}{\partial t} + \mathbf{u} \cdot \nabla\alpha_2 = \alpha_1\alpha_2 \frac{\rho_1 a_1^2 - \rho_2 a_2^2}{\alpha_1\rho_2 a_2^2 + \alpha_2\rho_1 a_1^2}\, \nabla \cdot \mathbf{u} + \mathcal{R}, \tag{30e}$$

where $\hat{\mathcal{R}} = \hat{\mathcal{R}}_1 + \hat{\mathcal{R}}_2$.

4. Numerical method

The governing equations are discretized on a fixed Cartesian mesh with an established block-structured Adaptive Mesh Refinement (AMR) [59,60]. To achieve maximum resolution near the interface, refinement is based on the scaled gradient

$$\Delta|\nabla\alpha_2| > \delta, \tag{31}$$

where Δ is the geometrically averaged grid spacing. We take $\delta = 10^{-6}$ in the present simulations. When (31) is satisfied, the grid is refined an additional level and the solution is interpolated to the new grid.

The compressible flow equations are solved using the finite-volume method with the well-known reconstruct–evolve-average (REA) technique [61,62]. A total variation diminishing third-order Runge–Kutta method [63] is used for time integration. The reduced system (30a)–(30e) is not exactly conservative in divergence form due to the advective form of the volume fraction equation and the regularization terms. In the presence of discontinuities, the numerical solution of a non-conservative hyperbolic system poses computational difficulties owing to the lack of generalized weak solutions that accurately define the shock relations. Even with approximate jump conditions [64], it is difficult to develop a path-conservative numerical scheme that converges to the correct solution [65–68]. A first step toward developing a numerical method to solve (30e) is to recast it as

$$\frac{\partial \alpha_2}{\partial t} + \nabla \cdot (\alpha_2\mathbf{u}) = K\,\nabla \cdot \mathbf{u} + \mathcal{R}(\alpha_2), \tag{32}$$

$$K = \frac{\alpha_2\rho_1 a_1^2}{\alpha_1\rho_2 a_2^2 + \alpha_2\rho_1 a_1^2}. \tag{33}$$

The next step involves volume averaging of the governing system of equations, in which, we use the following approximation to numerically compute the right-hand side of (32),

$$\frac{1}{V_{ijk}} \int_{V_{ijk}} (K\nabla \cdot \mathbf{u})\,\mathrm{d}V \approx \frac{1}{V_{ijk}} K_{ijk} \int_{S_{ijk}} \mathbf{u} \cdot \mathrm{d}\mathbf{S}, \tag{34}$$

where subscript ijk refers to the average values at the corresponding computational cell; V and S denote volume and surface of the cell, respectively. It should be noted that (34) is at best second-order accurate near the interface. However, it does not alter the overall spatial accuracy of our method because the shock-capturing scheme will invariably reduce the method to sub-first-order accurate near sharp flow field transitions or discontinuities [61].

We use a centered second-order approximation to evaluate $\mathcal{R}$ in (30a)–(30e). The Riemann problem is solved approximately using the HLLC method [62,69,70], though this necessitates special care in the discrete evolution of the interface function to ensure compatibility with the Euler system [49]. Johnsen and Colonius [49] have proposed an adaptation of the HLLC Riemann solver to the volume fraction evolution for the diffuse interface method based on the advection model [39]. We use the equivalent adaptation for the asymptotically reduced model. For spatial reconstruction, we use a WENO method [71–73], but we observed only marginal improvement in results upon implementing the two-point (fourth-order accurate)

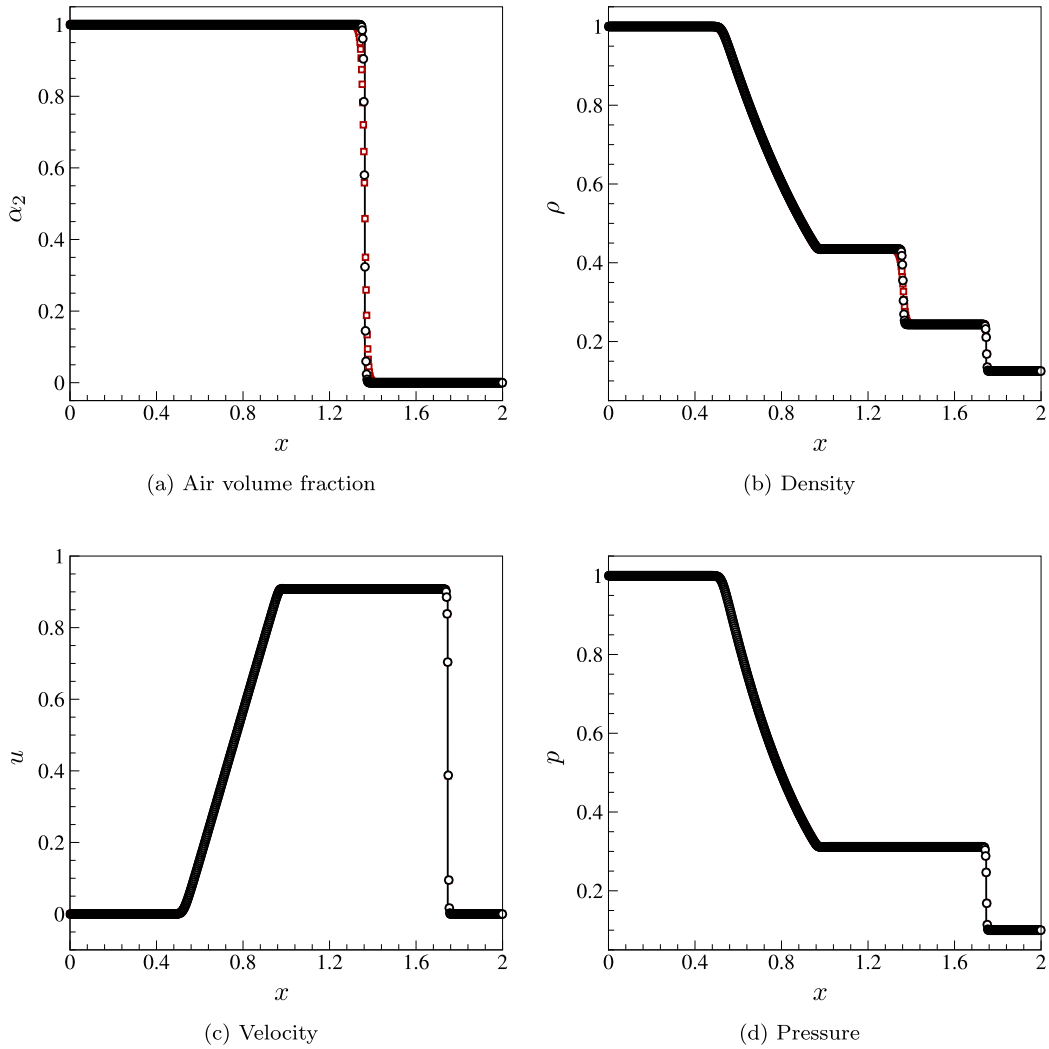

Fig. 3. Simulation results for the air–helium shock-tube problem without (□) and with (○) $\mathcal{R}$ compared with the exact solution (−).

Gaussian integration proposed by Titarev and Toro [74] for finite-volume WENO methods. Therefore, for computational efficiency, we use a fifth-order accurate WENO reconstruction without the Gaussian integration in this study. Reconstruction is performed on primitive variables to avoid spurious pressure oscillations at the interface [49]. We show in Appendix B that appropriate interface conditions for equilibrium flows are preserved with our method, despite the regularization.

5. Tests and validations

We first demonstrate convergence of our method on one-dimensional problems on one-dimensional meshes. This is followed by simulations of free-space and near-wall bubble collapses. A uniform Cartesian mesh is taken in all the simulations, with the regularization parameter $\epsilon = 0.75\Delta x_{\min}$ in (20), where $\Delta x_{\min}$ denotes the finest AMR mesh spacing. Characteristic based non-reflecting boundary conditions are applied at far-field boundaries [75]. The one-dimensional simulations are carried out without AMR, with extrapolation boundary conditions, and employing second-order spatial reconstruction using the minmod limiter. Three-dimensional simulations are performed with fifth-order WENO spatial reconstruction.

5.1. Air–helium shock-tube problem

We consider the initial condition [48]

$$(\rho, u, p, \alpha_2) = \begin{cases} (1, 0, 1, 1) & \text{for } 0 \leqslant x \leqslant 1, \\ (0.125, 0, 0.1, 0) & \text{otherwise,} \end{cases}$$

Table 1
Convergence of air volume fraction (α_2) for the air–helium shock-tube problem. The error for any solution variable ϕ is defined by $\sum_i^n |\phi_{i,\text{simulation}} - \phi_{i,\text{exact}}|/n$, where n is the number of grid cells.

Grid cells	$\mathcal{R} = 0$		With $\mathcal{R}$	
	Error	Order	Error	Order
200	1.10×10^{-2}		6.80×10^{-3}	
400	7.14×10^{-3}	0.62	3.80×10^{-3}	0.84
800	4.48×10^{-3}	0.67	1.70×10^{-3}	1.16
1600	2.85×10^{-3}	0.65	8.47×10^{-4}	1.01

Table 2
Conservation of mass ($\mathcal{M} \equiv \int \rho \, \mathrm{d}V$) and energy ($\mathcal{E} \equiv \int \rho E \, \mathrm{d}V$) for the air–helium shock-tube problem with $\Delta(\cdot) \equiv |(\cdot)_{\text{initial}} - (\cdot)_{\text{final}}|/(\cdot)_{\text{initial}}$.

Grid cells	$\mathcal{R} = 0$		With $\mathcal{R}$	
	$\Delta\mathcal{M}$	$\Delta\mathcal{E}$	$\Delta\mathcal{M}$	$\Delta\mathcal{E}$
200	5.05×10^{-15}	1.13×10^{-14}	2.54×10^{-4}	4.67×10^{-5}
400	8.84×10^{-15}	8.31×10^{-15}	2.20×10^{-4}	3.97×10^{-5}
800	1.54×10^{-14}	2.81×10^{-14}	1.12×10^{-4}	2.01×10^{-5}
1600	2.54×10^{-14}	2.39×10^{-14}	5.67×10^{-5}	1.02×10^{-5}

Table 3
Convergence of mixture density (ρ) for the air–helium shock-tube problem. (Error is defined in Table 1.)

Grid cells	$\mathcal{R} = 0$		With $\mathcal{R}$	
	Error	Order	Error	Order
200	4.43×10^{-3}		3.65×10^{-3}	
400	2.63×10^{-3}	0.75	2.00×10^{-3}	0.87
800	1.45×10^{-3}	0.87	9.17×10^{-4}	1.12
1600	8.54×10^{-4}	0.76	4.70×10^{-4}	0.96

Table 4
Convergence of volume-specific total energy (ρE) for the air–helium shock-tube problem. (Error is defined in Table 1.)

Grid cells	$\mathcal{R} = 0$		With $\mathcal{R}$	
	Error	Order	Error	Order
200	1.08×10^{-2}		9.40×10^{-3}	
400	6.17×10^{-3}	0.81	5.04×10^{-3}	0.90
800	3.29×10^{-3}	0.90	2.36×10^{-3}	1.10
1600	1.88×10^{-3}	0.81	1.20×10^{-3}	0.97

where α_2 denotes the air volume fraction. Air and helium are treated as ideal gases with $\gamma = 1.4$ and 1.6, respectively. The interface regularization is activated after the interface thickness as defined in (2) becomes greater than the grid spacing. Simulation results using 800 grid cells at $t = 0.4$ with and without $\mathcal{R}$ are compared with the exact solution in Fig. 3. The resolution study in Table 1 demonstrates better convergence of the new method.

It should be noted that the volume fraction transport equation in the underlying model of Kapila et al. [38] is not in conservation form, which leads to non-conservative products on the right-hand side of the entire system in (A.16a)–(A.16e). Shukla et al. [50] showed that if the numerical implementation without $\mathcal{R}$ is conservative, then the density regularization is asymptotically mass conservative with mesh refinement provided it is done according to (A.16a) and (A.16b). The present model has analogous terms in the right-hand side of the entire system, yielding asymptotic conservation to mixture mass, momentum and energy. This is demonstrated in Table 2, which shows better mass and energy conservation with $\mathcal{R}$ upon mesh refinement. We further show in Tables 3 and 4 that even though mixture mass and energy have better conservation without regularization, the numerical smearing hampers convergence to the correct solution of these quantities as well.

5.2. Isolated single-bubble collapse: one-dimensional simulation

We consider the collapse of an air bubble in water under an initial pressure ratio $p_\infty/p_0 = 10$, with the bubble at its maximum radius $R_0 = 1$ mm at $t = 0$. The simulation domain is large enough to avoid boundary effects: $0 \leqslant r \leqslant 160 \times R_0$. The initial pressure profile in water $p(r)$ is obtained from the Rayleigh–Plesset model [10]:

$$\rho = \rho_1\alpha_1 + \rho_2\alpha_2,$$
$$u = 0,$$

Table 5
Convergence of air volume fraction (α_2) for the isolated single-bubble collapse at $t = 100$ μs. (Error is defined in Table 1.)

$R_0/\Delta r$	$\mathcal{R} = 0$		With $\mathcal{R}$	
	Error	Order	Error	Order
12.5	7.65×10^{-4}		6.82×10^{-4}	
25	5.11×10^{-4}	0.58	3.77×10^{-4}	0.85
50	2.98×10^{-4}	0.78	1.60×10^{-4}	1.23
100	1.94×10^{-4}	0.62	7.74×10^{-5}	1.05

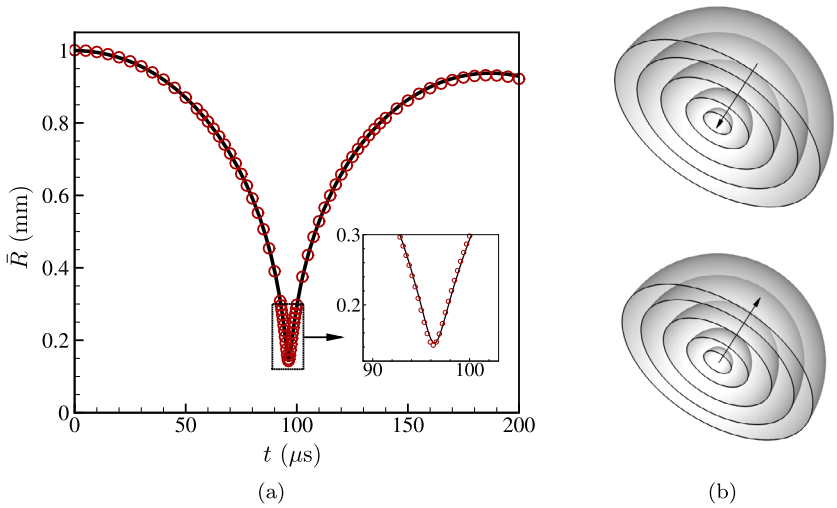

Fig. 4. (a) Radius profile comparison with the Keller and Miksis [53] solution (—), for isolated single-bubble collapse under a pressure ratio of 25. (b) Bubble shapes at various times during collapse (top) and re-expansion (bottom) obtained from our overall numerical scheme. The innermost and outermost surfaces correspond to the minimum and maximum volumes, respectively. Arrows indicate increasing time.

$$p = \begin{cases} p_0 & \text{for } 0 \leqslant r \leqslant R_0, \\ p(r) = p_\infty + \frac{R_0}{r}(p_0 - p_\infty) & \text{otherwise,} \end{cases}$$

$$\alpha_2 = \frac{1}{2}\left[1 - \tanh\left(\frac{r - R_0}{2\epsilon}\right)\right],$$

where α_2 denotes the air volume fraction, $\rho_1 = 1000$ kg/m^3, and $\rho_2 = 0.19$ kg/m^3. Three-dimensional simulations for the same problem were discussed in Section 2. Table 5 demonstrates improvement in convergence properties of the numerical scheme upon incorporating $\mathcal{R}$.

5.3. Isolated single-bubble collapse: three-dimensional simulation

We next consider the collapse of an air bubble in water under a pressure ratio $p_\infty/p_0 = 25$, with $\bar{R}_{\min}/\Delta x_{\min} \approx 7.3$. Without AMR, the total mesh size required to maintain the finest resolution used in this simulation would have been $2048^3 \approx 86 \times 10^8$, while the number of grid cells we required with AMR at $t = 0$ is about 7×10^6. Fig. 4 compares the radial profiles obtained from the simulation with the KM solution. The bubble shapes obtained from the overall numerical scheme with regularization are also shown in Fig. 4. Higher pressure ratios are, of course, more challenging both because the bubble becomes much smaller and the radiated acoustic energy is more important. Fig. 5 shows a similar collapse, but with $p_\infty/p_0 = 100$, using $\bar{R}_{\min}/\Delta x_{\min} \approx 5.8$. Both the average bubble-interior pressure and the radius history agree well with theoretical predictions despite a factor of 1.7×10^5 change in the interior pressure. It is also clear that even the rebound is accurately predicted.

5.4. Near-wall single-bubble collapse

Finally, we consider the expansion and collapse of a gas bubble whose initial center is $d = 1.8$ mm away from a perfectly rigid wall (Fig. 6). At $t = 0$, the bubble is at its minimum radius ($R_0 = 0.5$ mm) under an initial pressure of 50 MPa, while the ambient water is initially at a uniform pressure (p_∞) of 10 MPa. The wall breaks the spherical symmetry, and an equivalent radius $\bar{R} = (3V/4\pi)^{1/3}$ is used to discuss the results. For this test case, $R_0/\Delta x_{\min} \approx 25.6$. Fig. 7 shows radial profile and volume fraction contours (at three successive minima) obtained from the simulations, showing the benefits of

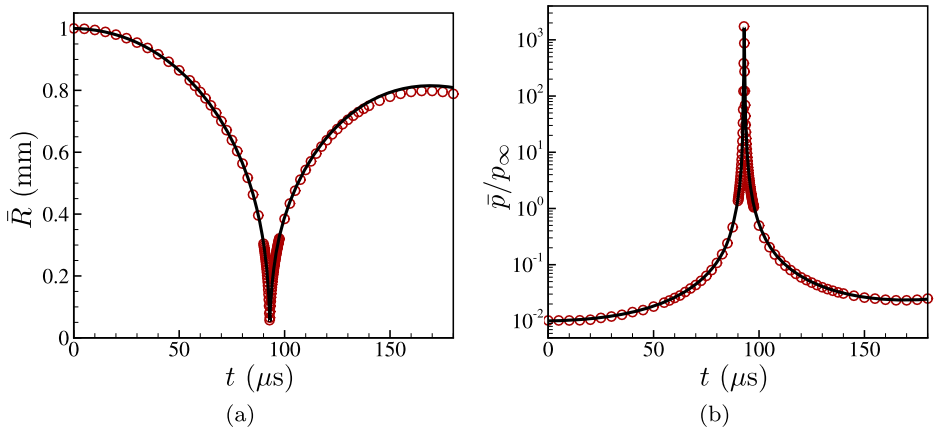

Fig. 5. Radius (a) and pressure (b) profiles obtained from the new model compared with the Keller and Miksis [53] solution (—), for isolated single-bubble collapse under a pressure ratio of 100.

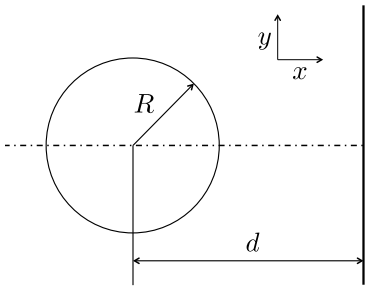

Fig. 6. Schematic of the arrangement for the near-wall collapse.

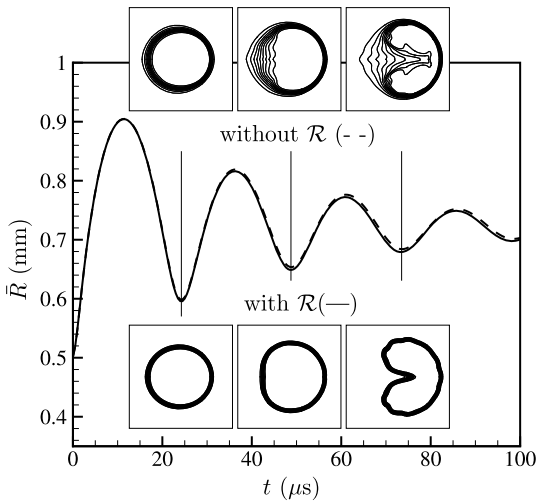

Fig. 7. Radius history for $\mathcal{R} = 0$ and the new model for the near-wall single-bubble expansion and collapse with an initial pressure ratio of 5. The insets show corresponding volume fraction contours (ranging from 0.1 to 0.9) at three successive minima.

including $\mathcal{R}$ in the analysis. While the domain integrals of gas volume fraction agree, consistent with the spherical results, visualization shows that without the regularization term the interface is both diffused to the same scale as the bubble shape and, in places, thinner than its target thickness. This spurious behavior increases obviously during the course of the simulation.

The smearing of the volume fraction field suppresses the kinetic energy of the jet that penetrates the bubble, which can be anticipated to be important for predictions of damage [10,11] (in marine applications) or injury [76] (in bio-medical ultrasound). To investigate this, we consider a test case with more asymmetry due to closer wall proximity. The bubble, in

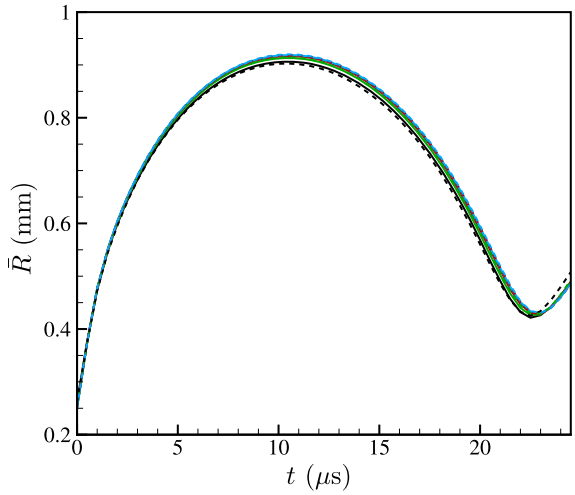

Fig. 8. Radius history for $\mathcal{R} = 0$ (- -) and the new model (−) for the near-wall single-bubble expansion and collapse for an initial pressure ratio of 50 with $R_0/\Delta x_{\min} \approx 6.4$, 12.8, 25.6, and 51.2.

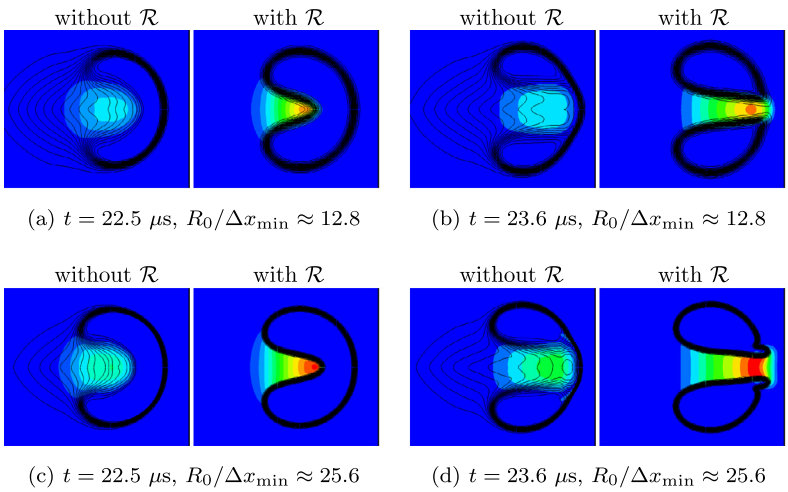

Fig. 9. Colors of normalized specific kinetic energy, and volume fraction contours (lines). Volume fraction contours range from 0.05 to 0.95; kinetic energy contours range from 1 to 13 in (a) and (c), and 1 to 9 in (b) and (d).

this case, has a smaller initial radius (0.25 mm), and is placed closer to the wall (1.1 mm), with a higher initial interior pressure (500 MPa). Fig. 8 shows good equivalent radius agreement between the two models in terms of total gas volume fraction. However, without $\mathcal{R}$, the distal surface is obviously smeared, with the consequence of a significantly weaker liquid jet (Fig. 9). This prevents the jet from fully penetrating the bubble. To quantify this, the spatial profile of normalized volume-specific kinetic energy ($\rho|\mathbf{u}|^2/2p_\infty$) along the symmetry axis is plotted versus time in Fig. 10. It is also clear that increasing resolution shows apparent global convergence for the new method, whereas no convergence yet (though it might be expected to be the correct trend) for $\mathcal{R} = 0$. It would be prohibitively expensive to converge the method without regularization.

The stronger and steeper jet, obtained from the new model with regularization, penetrates though the bubble, and upon impact on the proximal bubble surface emits a shock wave. To visualize this phenomenon, Fig. 11 shows contours of ψ [45]:

$$\psi = \exp\left(-50\frac{|\nabla\rho|}{|\nabla\rho|_{\max}}\right). \tag{36}$$

In Fig. 11, from left to right, the jet hits the liquid layer between the bubble and the wall in the first contour plot, the emitted shock wave reaches the wall in the second one, and the reflected wave interacts with the bubble in the third subfigure. The model without regularization fails to capture this phenomenon.

It is clear that a sharper and steeper jet kinetic energy will lead to a more focussed impact with higher wall pressure p_w. To examine this further, in Fig. 12, we plot the normalized impulse

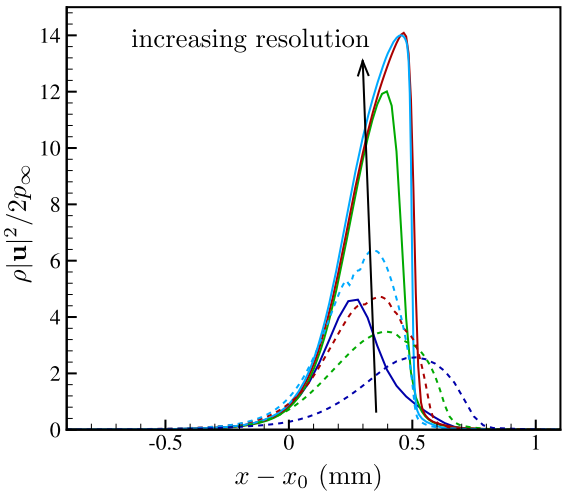

Fig. 10. Normalized specific kinetic energy along the axis of symmetry (the x-axis) at $t = 22.2$ μs for $\mathcal{R} = 0$ (dashed) and the new model (solid) with $R_0/\Delta x_{\min} \approx 6.4$, 12.8, 25.6, and 51.2. (x_0 is the x-coordinate of the bubble center at $t = 0$.)

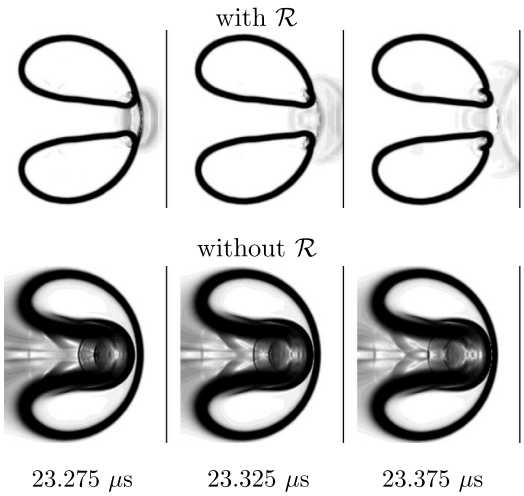

Fig. 11. Contours of ψ in (36) [45] for $\mathcal{R} = 0$ and the new model using $R_0/\Delta x_{\min} \approx 51.2$.

$$I_w = \int_{t_1}^{t_2} \frac{p_w - p_\infty}{p_\infty}\, \mathrm{d}t, \tag{37}$$

for $t_1 = 21.0$ μs and $t_2 = 24.5$ μs along the wall y-axis. I_w also appears converged globally with the new model and at a significantly higher value than the corresponding simulations with $\mathcal{R} = 0$.

6. Conclusion

An interface regularization scheme consistent with the first-order non-equilibrium mixture model is developed for bubble dynamics and other high-speed, multi-fluid flows. Smearing of the interface in the diffuse interface or mixture approach renders the solutions incorrect at long times. The interface sharpening approach of Shukla et al. [50] keeps the interface thickness fixed, but leads to qualitatively wrongs results due to thermodynamic inconsistencies. We have re-crafted the asymptotic multi-fluid formulation of [38,40] to incorporate the immiscibility condition into the model in a thermodynamically consistent fashion. This reduces a general seven-equation two-fluid compressible flow model to a five-equation model including interface regularization terms. The analysis is performed for general fluids whose states are fixed by two thermodynamic variables. The regularization operator is incorporated into the continuum equations, and is consequently independent of the underlying numerical scheme.

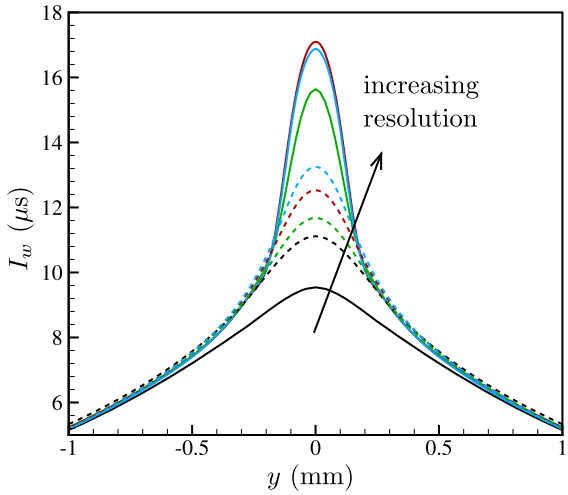

Fig. 12. Variation of I_w in (37) along the wall for $\mathcal{R} = 0$ (dashed) and the new model (solid) with $R_0/\Delta x_{\min} \approx 6.4$, 12.8, 25.6, and 51.2.

Upon establishing consistency and convergence of the model, we tested it on three-dimensional bubble collapses employing an AMR framework built on a fifth-order WENO method. We obtained excellent agreement of the simulations results with the spherically symmetric semi-analytic models for the free-space bubble collapses. The new model consistently preserves fluid immiscibility with superior convergence properties. The utility of the regularization scheme is further realized in the near-wall bubble collapses, for which, the new model prevents numerical smearing of the jet kinetic energy leading to stronger and converged jet impacts on the wall.

Acknowledgements

Portions of this work were supported by NIH grant PO1-DK043881.

Appendix A. Asymptotic analysis

To reduce (7a)–(7g) in the limit of zero relaxation time, we seek an asymptotic solution of the form

$$(s_1, s_2, \mathbf{u}_1, \mathbf{u}_2, p_1, p_2, \alpha_2) = \mathbf{q}^{(0)} + \delta\,\mathbf{q}^{(1)} + \cdots, \tag{A.1}$$

where δ is such that

$$\delta \sim \frac{1}{\lambda} \sim \frac{1}{\mu}. \tag{A.2}$$

Assuming

$$\mathcal{R}\big(\alpha_2^{(0)}\big) \text{ to be } \mathcal{O}(1),$$

retaining terms to $\mathcal{O}(1/\delta)$, and dropping the superscript notation, we arrive at

$$\mu(p_{\mathrm{I}} - p_1)(p_2 - p_1) + \lambda(\mathbf{u}_{\mathrm{I}} - \mathbf{u}_1)\cdot(\mathbf{u}_2 - \mathbf{u}_1) = 0, \tag{A.3a}$$

$$\mu(p_{\mathrm{I}} - p_2)(p_1 - p_2) + \lambda(\mathbf{u}_{\mathrm{I}} - \mathbf{u}_2)\cdot(\mathbf{u}_1 - \mathbf{u}_2) = 0, \tag{A.3b}$$

$$\lambda(\mathbf{u}_2 - \mathbf{u}_1) = 0, \tag{A.3c}$$

$$\lambda(\mathbf{u}_1 - \mathbf{u}_2) = 0, \tag{A.3d}$$

$$\mu\rho_1 a_{1\mathrm{I}}^2(p_2 - p_1) + \lambda\sigma_1(\mathbf{u}_{\mathrm{I}} - \mathbf{u}_1)\cdot(\mathbf{u}_2 - \mathbf{u}_1) = 0, \tag{A.3e}$$

$$\mu\rho_2 a_{2\mathrm{I}}^2(p_1 - p_2) + \lambda\sigma_2(\mathbf{u}_{\mathrm{I}} - \mathbf{u}_2)\cdot(\mathbf{u}_1 - \mathbf{u}_2) = 0, \tag{A.3f}$$

$$\mu(p_2 - p_1) = 0, \tag{A.3g}$$

which gives,

$$\mathbf{u}_{\mathrm{I}} = \mathbf{u}_1 = \mathbf{u}_2 = \mathbf{u} \quad \text{(equilibrium velocity)}, \tag{A.4}$$

$$p_{\mathrm{I}} = p_1 = p_2 = p \quad \text{(equilibrium pressure)}. \tag{A.5}$$

To $\mathcal{O}(1)$, using (A.4) and (A.5), we obtain

$$\frac{\mathrm{D}s_1}{\mathrm{D}t} = 0, \tag{A.6a}$$

$$\frac{\mathrm{D}s_2}{\mathrm{D}t} = 0, \tag{A.6b}$$

$$\alpha_1 \rho_1 \frac{\mathrm{D}\mathbf{u}}{\mathrm{D}t} + \alpha_1 \nabla p = \lambda\delta\big(\mathbf{u}_2^{(1)} - \mathbf{u}_1^{(1)}\big), \tag{A.6c}$$

$$\alpha_2 \rho_2 \frac{\mathrm{D}\mathbf{u}}{\mathrm{D}t} + \alpha_2 \nabla p = \lambda\delta\big(\mathbf{u}_1^{(1)} - \mathbf{u}_2^{(1)}\big), \tag{A.6d}$$

$$\alpha_1 \frac{\mathrm{D}p}{\mathrm{D}t} + \alpha_1 \rho_1 a_1^2 \nabla \cdot \mathbf{u} = \mu\delta\rho_1 a_1^2 \big(p_2^{(1)} - p_1^{(1)}\big), \tag{A.6e}$$

$$\alpha_2 \frac{\mathrm{D}p}{\mathrm{D}t} + \alpha_2 \rho_2 a_2^2 \nabla \cdot \mathbf{u} = \mu\delta\rho_2 a_2^2 \big(p_1^{(1)} - p_2^{(1)}\big), \tag{A.6f}$$

$$\frac{\mathrm{D}\alpha_2}{\mathrm{D}t} = \mu\delta\big(p_2^{(1)} - p_1^{(1)}\big) + \mathcal{R}(\alpha_2). \tag{A.6g}$$

Elimination of

$$\lambda\delta\big(\mathbf{u}_2^{(1)} - \mathbf{u}_1^{(1)}\big) \quad \text{and} \quad \mu\delta\big(p_2^{(1)} - p_1^{(1)}\big),$$

from (A.6a)–(A.6g), gives

$$\frac{\mathrm{D}s_1}{\mathrm{D}t} = 0, \tag{A.7a}$$

$$\frac{\mathrm{D}s_2}{\mathrm{D}t} = 0, \tag{A.7b}$$

$$\frac{\mathrm{D}\mathbf{u}}{\mathrm{D}t} + \frac{1}{\rho} \nabla p = 0, \tag{A.7c}$$

$$\frac{\mathrm{D}p}{\mathrm{D}t} + \rho a^2 \nabla \cdot \mathbf{u} = 0, \tag{A.7d}$$

$$\frac{\mathrm{D}\alpha_2}{\mathrm{D}t} = \alpha_1\alpha_2 \frac{\rho_1 a_1^2 - \rho_2 a_2^2}{\alpha_1 \rho_2 a_2^2 + \alpha_2 \rho_1 a_1^2} \nabla \cdot \mathbf{u} + \mathcal{R}(\alpha_2), \tag{A.7e}$$

where ρ and a are as defined in (15) and (18), respectively.

We now have the system in terms of $\mathbf{P} = (s_1, s_2, u, v, w, p, \alpha_2)^{\mathrm{t}}$:

$$\frac{\partial \mathbf{P}}{\partial t} + \mathbf{F}\frac{\partial \mathbf{P}}{\partial x} + \mathbf{G}\frac{\partial \mathbf{P}}{\partial y} + \mathbf{H}\frac{\partial \mathbf{P}}{\partial z} = \mathbf{R}, \tag{A.8}$$

where

$$\mathbf{F} = \begin{pmatrix} u & 0 & 0 & 0 & 0 & 0 & 0 \\ 0 & u & 0 & 0 & 0 & 0 & 0 \\ 0 & 0 & u & 0 & 0 & \frac{1}{\rho} & 0 \\ 0 & 0 & 0 & u & 0 & 0 & 0 \\ 0 & 0 & 0 & 0 & u & 0 & 0 \\ 0 & 0 & \rho a^2 & 0 & 0 & u & 0 \\ 0 & 0 & -\beta & 0 & 0 & 0 & u \end{pmatrix}, \tag{A.9}$$

with

$$\beta = \alpha_1\alpha_2 \frac{\rho_1 a_1^2 - \rho_2 a_2^2}{\alpha_1 \rho_2 a_2^2 + \alpha_2 \rho_1 a_1^2}, \tag{A.10}$$

and

$$\mathbf{R} = \big(0, 0, 0, 0, 0, 0, \mathcal{R}(\alpha_2)\big)^{\mathrm{t}}, \tag{A.11}$$

where $\mathbf{G}$ and $\mathbf{H}$ are defined similarly. Note that we focus only on $\mathbf{F}$ in this analysis. The objective at this stage is to write the system in terms of the quasi-conservative variables, $\mathbf{Q} = (\rho_1\alpha_1, \rho_2\alpha_2, \rho u, \rho v, \rho w, \rho E, \alpha_2)^{\mathrm{t}}$, where ρE is as defined in (16). To this end, we first construct the transformation matrix $\mathbf{B} = \partial\mathbf{Q}/\partial\mathbf{P}$, so that (A.8) can be equivalently written as

$$\frac{\partial \mathbf{Q}}{\partial t} + \mathbf{BFB}^{-1}\frac{\partial \mathbf{Q}}{\partial x} + \mathbf{BGB}^{-1}\frac{\partial \mathbf{Q}}{\partial y} + \mathbf{BHB}^{-1}\frac{\partial \mathbf{Q}}{\partial z} = \mathbf{BR}. \tag{A.12}$$

For fluids whose states are fixed by two thermodynamic variables, we first invoke Gibb's relation to obtain the partial derivates needed to construct $\mathbf{B}$:

$$\begin{aligned}
&\left(\frac{\partial \rho_k}{\partial s_k}\right)_p = -\frac{T_k\rho_k\sigma_k}{a_k^2}, \qquad \left(\frac{\partial \rho_k}{\partial p}\right)_{s_k} = \frac{1}{a_k^2},\\
&\left(\frac{\partial e_k}{\partial s_k}\right)_p = -\frac{T_k\rho_k\sigma_k\xi_k}{a_k^2}, \qquad \left(\frac{\partial e_k}{\partial p}\right)_{s_k} = \frac{p_k}{a_k^2\rho_k^2},
\end{aligned} \tag{A.13}$$

where

$$\xi_k = \left(\frac{\partial e_k}{\partial \rho_k}\right)_p = \frac{1}{\rho_k}\left(\frac{p}{\rho_k} - \frac{a_k^2}{\sigma_k}\right), \tag{A.14}$$

from which, we obtain

$$\begin{aligned}
&\frac{\partial \alpha_2}{\partial \mathbf{P}} = (0,0,0,0,0,0,1),\\
&\frac{\partial \rho_1}{\partial \mathbf{P}} = \left(-\frac{\rho_1\sigma_1T_1}{a_1^2}, 0,0,0,0, \frac{1}{a_1^2}, 0\right),\\
&\frac{\partial \rho_2}{\partial \mathbf{P}} = \left(0, -\frac{\rho_2\sigma_2T_2}{a_2^2}, 0,0,0, \frac{1}{a_2^2}, 0\right),\\
&\frac{\partial \alpha_1\rho_1}{\partial \mathbf{P}} = \alpha_1\frac{\partial \rho_1}{\partial \mathbf{P}} + (0,0,0,0,0,0,-\rho_1),\\
&\frac{\partial \alpha_2\rho_2}{\partial \mathbf{P}} = \alpha_2\frac{\partial \rho_2}{\partial \mathbf{P}} + (0,0,0,\ 0,0,0,\rho_2),\\
&\frac{\partial \rho}{\partial \mathbf{P}} = \frac{\partial \alpha_1\rho_1}{\partial \mathbf{P}} + \frac{\partial \alpha_2\rho_2}{\partial \mathbf{P}},\\
&\frac{\partial \rho u}{\partial \mathbf{P}} = u\frac{\partial \rho}{\partial \mathbf{P}} + \rho(0,0,1,0,0,0,0),\\
&\frac{\partial \rho v}{\partial \mathbf{P}} = v\frac{\partial \rho}{\partial \mathbf{P}} + \rho(0,0,0,1,0,0,0),\\
&\frac{\partial \rho w}{\partial \mathbf{P}} = w\frac{\partial \rho}{\partial \mathbf{P}} + \rho(0,0,0,0,\ 1,0,0),\\
&\frac{\partial \rho \kappa}{\partial \mathbf{P}} = \kappa\frac{\partial \rho}{\partial \mathbf{P}} + \rho(0,0,u,v,w,0,0),\\
&\frac{\partial \rho_1 e_1}{\partial \mathbf{P}} = \left(-\frac{(\rho_1\xi_1+e_1)T_1\rho_1\sigma_1}{a_1^2}, 0,0,0,0, \frac{e_1\rho_1+p}{\rho_1a_1^2}, 0\right),\\
&\frac{\partial \rho_2 e_2}{\partial \mathbf{P}} = \left(0, -\frac{(\rho_2\xi_2+e_2)T_2\rho_2\sigma_2}{a_2^2}, 0,0,0, \frac{e_2\rho_2+p}{\rho_2a_2^2}, 0\right),\\
&\frac{\partial \rho e}{\partial \mathbf{P}} = \alpha_1\frac{\partial \rho_1 e_1}{\partial \mathbf{P}} + \alpha_2\frac{\partial \rho_2 e_2}{\partial \mathbf{P}} + (0,0,0,0,0,0,\rho_2e_2-\rho_1e_1).
\end{aligned} \tag{A.15}$$

Substituting $\mathbf{B}$ in (A.12) yields the final quasi-conservative system for interfacial flows involving any two immiscible simple fluids:

$$\frac{\partial \alpha_1\rho_1}{\partial t} + \nabla\cdot(\alpha_1\rho_1\mathbf{u}) = -\rho_1\mathcal{R}(\alpha_2), \tag{A.16a}$$

$$\frac{\partial \alpha_2\rho_2}{\partial t} + \nabla\cdot(\alpha_2\rho_2\mathbf{u}) = \rho_2\mathcal{R}(\alpha_2), \tag{A.16b}$$

$$\frac{\partial \rho\mathbf{u}}{\partial t} + \nabla\cdot(\rho\mathbf{u}\otimes\mathbf{u}) + \nabla p = (\rho_2-\rho_1)\mathbf{u}\mathcal{R}(\alpha_2), \tag{A.16c}$$

$$\frac{\partial \rho E}{\partial t} + \nabla\cdot\big((\rho E+p)\mathbf{u}\big) = \big((\rho_2-\rho_1)\kappa+\eta\big)\mathcal{R}(\alpha_2), \tag{A.16d}$$

$$\frac{\partial \alpha_2}{\partial t} + \mathbf{u}\cdot\nabla\alpha_2 = \beta\nabla\cdot\mathbf{u} + \mathcal{R}(\alpha_2), \tag{A.16e}$$

where κ and β are as defined in (17) and (A.10), respectively, and $\eta = \rho_2e_2 - \rho_1e_1$.

Appendix B. Preservation of interface conditions for equilibrium flows

The utility of our approach is predicated upon maintaining mechanical equilibrium at interfaces. We confirm that this is exact for uniform conditions using a test problem proposed by Abgrall [43]. We check that uniform velocity, pressure and density at time t^n imply the same uniformity at time t^{n+1}, despite the interface regularization. To do this, we start with the quasi-conservative system (A.16a)–(A.16e) in discrete one-dimensional form for uniform pressure (p_0) and velocity (u_0),

$$(\alpha_1\rho_1)_i^{n+1} = (\alpha_1\rho_1)_i^n - \frac{\Delta t}{\Delta x}\Delta(\alpha_1\rho_1 u) - \Delta t\rho_{1,i}^n R, \tag{B.1a}$$

$$(\alpha_2\rho_2)_i^{n+1} = (\alpha_2\rho_2)_i^n - \frac{\Delta t}{\Delta x}\Delta(\alpha_2\rho_2 u) + \Delta t\rho_{2,i}^n R, \tag{B.1b}$$

$$(\rho u)_i^{n+1} = (\rho u)_i^n - \frac{\Delta t}{\Delta x}\Delta\left(\rho u^2\right) + \Delta t u_0\left(\rho_{2,i}^n - \rho_{1,i}^n\right)R, \tag{B.1c}$$

$$(\rho E)_i^{n+1} = (\rho E)_i^n - \frac{\Delta t}{\Delta x}\Delta(\rho E u) + \Delta t\left(\kappa_0\left(\rho_{2,i}^n - \rho_{1,i}^n\right) + \eta_i^n\right)R, \tag{B.1d}$$

$$(\alpha_2)_i^{n+1} = (\alpha_2)_i^n - \frac{\Delta t}{\Delta x}u_0\Delta(\alpha_2) + \Delta t R, \tag{B.1e}$$

where $\Delta(\cdot)$ denotes discrete flux for the hyperbolic part, and R denotes discrete regularization operator. Without loss of generality, we assume $u_0 > 0$ and choose simple upwind flux of the form

$$\Delta(\phi) = \phi_i^n - \phi_{i-1}^n. \tag{B.2}$$

(Extensions are available for more general $\Delta(\cdot)$ involving spatial reconstruction and Riemann solver [39,40,43,48,49].) Using (15), u_0((B.1a) + (B.1b))–(B.1c) yields

$$u_i^{n+1} = u_0, \tag{B.3}$$

and κ_0((B.1a) + (B.1b))–(B.1d) yields

$$(\rho e)_i^{n+1} = (\rho e)_i^n - \frac{\Delta t}{\Delta x}\Delta(\rho e u) + \Delta t\eta_i^n R, \tag{B.4}$$

where $\rho e = \rho E - \rho\kappa$. From (10) and (16),

$$\rho e = p(\Gamma_1\alpha_1 + \Gamma_2\alpha_2) + \Pi_1\alpha_1 + \Pi_2\alpha_2, \tag{B.5}$$

and

$$\eta = p(\Gamma_2 - \Gamma_1) + \Pi_2 - \Pi_1. \tag{B.6}$$

Using (14) and (B.6), (B.5) can be written as

$$\rho e = p\Gamma_1 + \Pi_1 + \eta\alpha_2, \tag{B.7}$$

which upon substitution in (B.4) yields

$$(p\Gamma_1 + \Pi_1 + \eta\alpha_2)_i^{n+1} = (p\Gamma_1 + \Pi_1 + \eta\alpha_2)_i^n - \frac{\Delta t}{\Delta x}\Delta\left((p\Gamma_1 + \Pi_1 + \eta\alpha_2)u\right) + \Delta t\eta_i^n R. \tag{B.8}$$

Since $\eta_i^n = p_0(\Gamma_2 - \Gamma_1) + \Pi_2 - \Pi_1$, η_i^n(B.1e)–(B.8) shows preserved uniformity:

$$p_i^{n+1} = p_0. \tag{B.9}$$

If density is also uniform ($\rho_1(x) = \rho_2(x) = \rho_0$), then using (14), ρ_0(B.1e) + (B.1a) and ρ_0(B.1e)–(B.1b) yield

$$\rho_{1,i}^{n+1} = \rho_{2,i}^{n+1} = \rho_0. \tag{B.10}$$

References

[1] J.R. Blake, D.C. Gibson, Cavitation bubbles near boundaries, Annu. Rev. Fluid Mech. 19 (1987) 99–123.
[2] J.P. Best, The formation of toroidal bubbles upon the collapse of transient cavities, J. Fluid Mech. 251 (1993) 79–107.
[3] S.G. Zhang, J.H. Duncan, G.L. Chahine, The final stage of the collapse of a cavitation bubble near a rigid wall, J. Fluid Mech. 257 (1993) 147–181.
[4] J.M. Boulton-Stone, J.R. Blake, Gas-bubbles bursting at a free-surface, J. Fluid Mech. 254 (1993) 437–466.
[5] J.R. Blake, M.C. Hooton, P.B. Robinson, R.P. Tong, Collapsing cavities, toroidal bubbles and jet impact, Philos. Trans. R. Soc. Lond. A 355 (1724) (1997) 537–550.
[6] Y.L. Zhang, K.S. Yeo, B.C. Khoo, C. Wang, 3D jet impact and toroidal bubbles, J. Comput. Phys. 166 (2) (2001) 336–360.

[7] E.A. Brujan, G.S. Keen, A. Vogel, J.R. Blake, The final stage of the collapse of a cavitation bubble close to a rigid boundary, Phys. Fluids 14 (1) (2002) 85–92.
[8] S.W. Fong, E. Klaseboer, C.K. Turangan, B.C. Khoo, K.C. Hung, Numerical analysis of a gas bubble near bio-materials in an ultrasound field, Ultrasound Med. Biol. 32 (6) (2006) 925–942.
[9] M. Lee, E. Klaseboer, B.C. Khoo, On the boundary integral method for the rebounding bubble, J. Fluid Mech. 570 (2007) 407–429.
[10] C.E. Brennen, Cavitation and Bubble Dynamics, Oxford University Press, New York, 1995.
[11] W. Lauterborn, T. Kurz, Physics of bubble oscillations, Rep. Progr. Phys. 73 (10) (2010) 106501.
[12] H. Luo, J.D. Baum, R. Löhner, On the computation of multi-material flows using ALE formulation, J. Comput. Phys. 194 (1) (2004) 304–328.
[13] G.J. Ball, B.P. Howell, T.G. Leighton, M.J. Schofield, Shock-induced collapse of a cylindrical air cavity in water: a free-Lagrange simulation, Shock Waves 10 (4) (2000) 265–276.
[14] C.K. Turangan, A.R. Jamaluddin, G.J. Ball, T.G. Leighton, Free-Lagrange simulations of the expansion and jetting collapse of air bubbles in water, J. Fluid Mech. 598 (2008) 1–25.
[15] I.L. Chern, J. Glimm, O. McBryan, B. Plohr, S. Yaniv, Front tracking for gas-dynamics, J. Comput. Phys. 62 (1) (1986) 83–110.
[16] J.P. Cocchi, R. Saurel, A Riemann problem based method for the resolution of compressible multimaterial flows, J. Comput. Phys. 137 (2) (1997) 265–298.
[17] J. Glimm, J.W. Grove, X.L. Li, K.M. Shyue, Y.N. Zeng, Q. Zhang, Three-dimensional front tracking, SIAM J. Sci. Comput. 19 (3) (1998) 703–727.
[18] G. Tryggvason, B. Bunner, A. Esmaeeli, D. Juric, N. Al-Rawahi, W. Tauber, J. Han, S. Nas, Y.J. Jan, A front-tracking method for the computations of multiphase flow, J. Comput. Phys. 169 (2) (2001) 708–759.
[19] S. Osher, R.P. Fedkiw, Level set methods: An overview and some recent results, J. Comput. Phys. 169 (2) (2001) 463–502.
[20] W. Mulder, S. Osher, J.A. Sethian, Computing interface motion in compressible gas-dynamics, J. Comput. Phys. 100 (2) (1992) 209–228.
[21] R.P. Fedkiw, T. Aslam, B. Merriman, S. Osher, A non-oscillatory Eulerian approach to interfaces in multimaterial flows (the ghost fluid method), J. Comput. Phys. 152 (2) (1999) 457–492.
[22] R.P. Fedkiw, T. Aslam, S.J. Xu, The ghost fluid method for deflagration and detonation discontinuities, J. Comput. Phys. 154 (2) (1999) 393–427.
[23] R.P. Fedkiw, Coupling an Eulerian fluid calculation to a Lagrangian solid calculation with the ghost fluid method, J. Comput. Phys. 175 (1) (2002) 200–224.
[24] T.G. Liu, B.C. Khoo, K.S. Yeo, Ghost fluid method for strong shock impacting on material interface, J. Comput. Phys. 190 (2) (2003) 651–681.
[25] T.G. Liu, B.C. Khoo, C.W. Wang, The ghost fluid method for compressible gas–water simulation, J. Comput. Phys. 204 (1) (2005) 193–221.
[26] X.Y. Hu, B.C. Khoo, N.A. Adams, F.L. Huang, A conservative interface method for compressible flows, J. Comput. Phys. 219 (2) (2006) 553–578.
[27] R.R. Nourgaliev, T.N. Dinh, T.G. Theofanous, Adaptive characteristics-based matching for compressible multifluid dynamics, J. Comput. Phys. 213 (2) (2006) 500–529.
[28] X.Y. Hu, N.A. Adams, G. Iaccarino, On the HLLC Riemann solver for interface interaction in compressible multi-fluid flow, J. Comput. Phys. 228 (17) (2009) 6572–6589.
[29] H. Terashima, G. Tryggvason, A front-tracking/ghost-fluid method for fluid interfaces in compressible flows, J. Comput. Phys. 228 (11) (2009) 4012–4037.
[30] S.K. Sambasivan, H.S. UdayKumar, Sharp interface simulations with Local Mesh Refinement for multi-material dynamics in strongly shocked flows, Comput. & Fluids 39 (9) (2010) 1456–1479.
[31] E. Lauer, X.Y. Hu, S. Hickel, N.A. Adams, Numerical modelling and investigation of symmetric and asymmetric cavitation bubble dynamics, Comput. & Fluids 69 (2012) 1–19.
[32] M.R. Baer, J.W. Nunziato, A two-phase mixture theory for the deflagration-to-detonation transition (DDT) in reactive granular materials, Int. J. Multiph. Flow 12 (6) (1986) 861–889.
[33] R. Saurel, R. Abgrall, A multiphase Godunov method for compressible multifluid and multiphase flows, J. Comput. Phys. 150 (2) (1999) 425–467.
[34] G.H. Miller, E.G. Puckett, A high-order Godunov method for multiple condensed phases, J. Comput. Phys. 128 (1) (1996) 134–164.
[35] P. Jenny, B. Muller, H. Thomann, Correction of conservative Euler solvers for gas mixtures, J. Comput. Phys. 132 (1) (1997) 91–107.
[36] J.W. Banks, D.W. Schwendeman, A.K. Kapila, W.D. Henshaw, A high-resolution Godunov method for compressible multi-material flow on overlapping grids, J. Comput. Phys. 223 (1) (2007) 262–297.
[37] C.H. Chang, M.S. Liou, A robust and accurate approach to computing compressible multiphase flow: Stratified flow model and AUSM$^+$-up scheme, J. Comput. Phys. 225 (1) (2007) 840–873.
[38] A.K. Kapila, R. Menikoff, J.B. Bdzil, S.F. Son, D.S. Stewart, Two-phase modeling of deflagration-to-detonation transition in granular materials: Reduced equations, Phys. Fluids 13 (10) (2001) 3002–3024.
[39] G. Allaire, S. Clerc, S. Kokh, A five-equation model for the simulation of interfaces between compressible fluids, J. Comput. Phys. 181 (2) (2002) 577–616.
[40] A. Murrone, H. Guillard, A five equation reduced model for compressible two phase flow problems, J. Comput. Phys. 202 (2) (2005) 664–698.
[41] R. Saurel, F. Petitpas, R. Abgrall, Modelling phase transition in metastable liquids: application to cavitating and flashing flows, J. Fluid Mech. 607 (2008) 313–350.
[42] R. Saurel, F. Petitpas, R.A. Berry, Simple and efficient relaxation methods for interfaces separating compressible fluids, cavitating flows and shocks in multiphase mixtures, J. Comput. Phys. 228 (5) (2009) 1678–1712.
[43] R. Abgrall, How to prevent pressure oscillations in multicomponent flow calculations: A quasi conservative approach, J. Comput. Phys. 125 (1) (1996) 150–160.
[44] S. Karni, Hybrid multifluid algorithms, SIAM J. Sci. Comput. 17 (5) (1996) 1019–1039.
[45] J.J. Quirk, S. Karni, On the dynamics of a shock–bubble interaction, J. Fluid Mech. 318 (1996) 129–163.
[46] K.M. Shyue, An efficient shock-capturing algorithm for compressible multicomponent problems, J. Comput. Phys. 142 (1) (1998) 208–242.
[47] R. Saurel, R. Abgrall, A simple method for compressible multifluid flows, SIAM J. Sci. Comput. 21 (3) (1999) 1115–1145.
[48] R. Abgrall, S. Karni, Computations of compressible multifluids, J. Comput. Phys. 169 (2) (2001) 594–623.
[49] E. Johnsen, T. Colonius, Implementation of WENO schemes in compressible multicomponent flow problems, J. Comput. Phys. 219 (2) (2006) 715–732.
[50] R.K. Shukla, C. Pantano, J.B. Freund, An interface capturing method for the simulation of multi-phase compressible flows, J. Comput. Phys. 229 (19) (2010) 7411–7439.
[51] K.K. So, X.Y. Hu, N.A. Adams, Anti-diffusion interface sharpening technique for two-phase compressible flow simulations, J. Comput. Phys. 231 (11) (2012) 4304–4323.
[52] S. Kokh, F. Lagoutière, An anti-diffusive numerical scheme for the simulation of interfaces between compressible fluids by means of a five-equation model, J. Comput. Phys. 229 (8) (2010) 2773–2809.
[53] J.B. Keller, M. Miksis, Bubble oscillations of large-amplitude, J. Acoust. Soc. Am. 68 (2) (1980) 628–633.
[54] A. Prosperetti, A. Lezzi, Bubble dynamics in a compressible liquid. Part 1. First-order theory, J. Fluid Mech. 168 (1986) 457–478.
[55] E. Olsson, G. Kreiss, A conservative level set method for two phase flow, J. Comput. Phys. 210 (1) (2005) 225–246.
[56] J.C. Adams, P.N. Swarztrauber, SPHEREPACK 3.0: A model development facility, Mon. Weather Rev. 127 (1999) 1872–1878.
[57] R. Menikoff, B.J. Plohr, The Riemann problem for fluid-flow of real materials, Rev. Mod. Phys. 61 (1) (1989) 75–130.

[58] E. Olsson, G. Kreiss, S. Zahedi, A conservative level set method for two phase flow II, J. Comput. Phys. 225 (1) (2007) 785–807.
[59] R. Deiterding, R. Radovitzky, S.P. Mauch, L. Noels, J.C. Cummings, D.I. Meiron, A virtual test facility for the efficient simulation of solid material response under strong shock and detonation wave loading, Eng. Comput. 22 (3–4) (2006) 325–347.
[60] M.J. Berger, J. Oliger, Adaptive mesh refinement for hyperbolic partial-differential equations, J. Comput. Phys. 53 (3) (1984) 484–512.
[61] R.J. Leveque, Finite Volume Methods for Hyperbolic Problems, Cambridge University Press, New York, 2002.
[62] E.F. Toro, Riemann Solvers and Numerical Methods for Fluid Dynamics, Springer, Berlin, 2006.
[63] S. Gottlieb, C.W. Shu, Total variation diminishing Runge–Kutta schemes, Math. Comp. 67 (1988) 73–85.
[64] R. Saurel, O. Le Metayer, J. Massoni, S. Gavrilyuk, Shock jump relations for multiphase mixtures with stiff mechanical relaxation, Shock Waves 16 (3) (2007) 209–232.
[65] C. Pares, Numerical methods for nonconservative hyperbolic systems: A theoretical framework, SIAM J. Numer. Anal. 44 (1) (2006) 300–321.
[66] M.J. Castro, P.G. LeFloch, M.L. Munoz-Ruiz, C. Pares, Why many theories of shock waves are necessary: Convergence error in formally path-consistent schemes, J. Comput. Phys. 227 (17) (2008) 8107–8129.
[67] R. Abgrall, S. Karni, A comment on the computation of non-conservative products, J. Comput. Phys. 229 (8) (2010) 2759–2763.
[68] M.L. Munoz-Ruiz, C. Pares, On the convergence and well-balanced property of path-conservative numerical schemes for systems of balance laws, J. Sci. Comput. 48 (1–3) (2011) 274–295.
[69] E.F. Toro, M. Spruce, W. Speares, Restoration of the contact surface in the HLL-Riemann solver, Shock Waves 4 (1994) 25–34.
[70] P. Batten, N. Clarke, C. Lambert, D.M. Causon, On the choice of wavespeeds for the HLLC Riemann solver, SIAM J. Sci. Comput. 18 (6) (1997) 1553–1570.
[71] X.D. Liu, S. Osher, T. Chan, Weighted essentially non-oscillatory schemes, J. Comput. Phys. 115 (1) (1994) 200–212.
[72] G.S. Jiang, C.W. Shu, Efficient implementation of weighted ENO schemes, J. Comput. Phys. 126 (1) (1996) 202–228.
[73] C.W. Shu, High order weighted essentially nonoscillatory schemes for convection dominated problems, SIAM Rev. 51 (1) (2009) 82–126.
[74] V.A. Titarev, E.F. Toro, Finite-volume WENO schemes for three-dimensional conservation laws, J. Comput. Phys. 201 (1) (2004) 238–260.
[75] C. Pantano, R. Deiterding, D.J. Hill, D.I. Pullin, A low numerical dissipation patch-based adaptive mesh refinement method for large-eddy simulation of compressible flows, J. Comput. Phys. 221 (1) (2007) 63–87.
[76] J.B. Freund, R.K. Shukla, A.P. Evan, Shock-induced bubble jetting into a viscous fluid with application to tissue injury in shock-wave lithotripsy, J. Acoust. Soc. Am. 126 (5) (2009) 2746–2756.